

A parametric study of the noise radiated by the flow around multiple bodies: direct noise computation of the influence of the separating distance in rod-airfoil flow configurations

J. Berland*, P. Lafon†

*Laboratoire de Mécanique des Structures Industrielles Durables (LaMSID)
UMR CNRS EDF 2832, Clamart, France*

F. Crouzet‡, F. Daude§

*Électricité de France R&D
Department of Applied Mechanics and Acoustics, Clamart, France*

C. Bailly¶

*Laboratoire de Mécanique des Fluides et Acoustique and Institut Universitaire de France
École Centrale de Lyon & UMR CNRS 5509, Ecully, France*

The sound radiated by an airfoil in the wake of a rod is predicted by means of compressible large-eddy (LES) simulation. The LES strategy is based on high-order spectral-like numerical methods to allow the direct noise calculation of the sound sources. Owing to the complexity of the geometry, an overset grid approach is implemented in order to tackle with turbulent flows around multiple solid bodies. First, the aerodynamic data as well as the acoustic far-field are thoroughly compared to the experimental data of Jacob *et al.* [J. Theoret. Comput. Fluid Dyn., 19(3), 2005] in order to demonstrate the accuracy of the present simulation. Then a parametric study of the influence of separating rod-airfoil distance on the flow regimes and on the acoustic radiation is performed.

I. Introduction

The present work is concerned with the numerical study of the sound generated by an airfoil placed in the wake of a rod. Rod-airfoil configurations are indeed believed to be a benchmark well-suited for numerical modeling of sound generation processes in turbomachines.¹⁹ At appropriate operating conditions, vortex shedding in the wake of the rod can exhibit significant three dimensional effects, and a spectral broadening of the turbulent motions around the shedding frequency commonly occurs.²⁸ The impingement of these vortical structures on the leading edge of the airfoil generates sound sources, which are similar to the discrete frequency tones and broadband noise observed in turbomachines: rotor blades indeed undergo unsteady pressure fluctuations and one may observe discrete frequency radiation consisting of pure tones at harmonics of the blade passing frequency.¹⁶ In addition, broadband noise is produced by the interaction of the solid surfaces with the turbulent wakes.

*Research Engineer

†Research Engineer, AIAA Senior Member, philippe.lafon@edf.fr

‡Research Engineer

§Research Engineer

¶Professor, AIAA Senior Member

The flow physics of the rod-airfoil case has been studied by means of experimental studies. Jacob *et al.*¹⁹ for instance provided an extensive database of the features of the interaction between a cylinder wake and an airfoil. Mean flow quantities, velocity spectra of the turbulent motions as well as pressure spectra in the far-field are available. In a similar manner, Takagi *et al.*²⁴ investigated the influence of the cylinder transverse location (perpendicular to the freestream flow direction) on the turbulent development of the flow around the airfoil and showed that it may have an impact on the radiated acoustic field.

Further knowledge on the details of the rod-airfoil configuration can be gained thanks to numerical simulations. Past developments in the Computational AeroAcoustic (CAA) field have indeed made possible the calculation of the noise radiated by turbulent flows.²⁷ CAA techniques can be sorted out following two main categories: hybrid and direct approaches. For hybrid calculation, the aerodynamic and the acoustic fields are computed during two separate stages. Turbulence dynamics is first calculated and the radiated sound is then deduced from these data using for instance an acoustic analogy formulation.²⁰ During the computation of the turbulent flow, noise generation phenomena are not taken into account and classical numerical techniques inherited from computational fluid dynamics can be used. Several attempts have already been made to predict sound spectra radiated by the flow around a rod-airfoil. Casalino *et al.*⁹ applied the Ffowcs Williams-Hawkings (FW-H) formulation¹⁴ to flow data provided by an unsteady RANS (Reynolds-Average Navier-Stokes) simulation. In a similar manner, Boudet *et al.*⁸ coupled a LES calculation with a FW-H acoustic analogy. More recently, Greschner *et al.*¹⁵ evaluated far-field pressure spectra thanks to a DES/FW-H (Detached Eddy Simulation) aeroacoustic approach. Though these former studies presented results in agreement with the experiments, hybrid methods unfortunately uncouple the aerodynamic and acoustic fields so that the details of the flow physics are more difficult to determine. Both aerodynamic and acoustic fluctuations are computed within a same run for direct approaches. The method, here referred to as direct noise calculation (DNC), does not require any modeling of the sound sources and hence provides reliable results. Even though it has been successfully applied to various flow configurations,^{2,6,13} performing a DNC is still a challenging task. High-order numerical techniques on structured grids are commonly used for CAA in order to accurately capture the large disparities of length scales and amplitudes of the aerodynamic and acoustic fluctuations.²⁵ In the case of flows around multiple bodies, high-order discretization tools are especially tedious to implement. For complex geometries, these difficulties can be circumvented using an overset grid approach.¹² The computational domain is divided into a set of overlapping structured grids. These body-fitted curvilinear meshes greatly ease the enforcement of boundary conditions and allow to simulate flow around various solid bodies. Flow data exchange between the grids can be carried out by means of high-order Lagrangian interpolation.²³ As concern turbulence modeling, the study of flows with Reynolds number of practical interest requires to perform compressible large eddy simulation (LES). In LES, only the larger scales are resolved and a subgrid scale model takes into account the effects of unresolved small wavelengths. It is then possible to deal with realistic turbulence configurations while keeping computational cost at a reasonable level. In the present work, to take account of the dissipation provided by the unresolved scales, a LES based on relaxation filtering (LES-RF) is performed.⁷ The idea is to minimize the dissipation at the larger scales while diffusing at small scales the drain of energy due to the turbulence energy cascade. Explicit spectral-like filtering is therefore applied to the conservative flow variables. The method has been successfully used in multiple applications.^{2,5}

The present study, which is a follow-up of a previous investigation,³ aims first at demonstrating the feasibility of the DNC, based on compressible LES, of the rod-airfoil flow configuration using high-order numerical methods on a set of overlapping structured curvilinear grids and then at applying this approach for a parametric study of the influence of the separating distance in the rod-airfoil configuration. So the experimental flow setup of Jacob *et al.*¹⁹ is first simulated by *Code_Safari*¹³ (Simulation of Aeroacoustics in Flows And with Resonance and Interaction) : a symmetric NACA0012 airfoil is located one chord downstream of a rod, whose wake contains both tonal and broadband fluctuations. The freestream Mach number M_∞ is 0.2. Then several simulations are carried out for 15 values of L/d , L being the gap between the cylinder and the airfoil and d being the cylinder diameter.

The outline of this paper is the following. The physical configuration, the numerical procedure and the simulation parameters are detailed in section II. Some results on the turbulent flow development and on the acoustic field for the reference configuration of Jacob *et al.*¹⁹ are presented in section III in order to validate the direct noise calculation approach. The parametric study of the influence of the separating rod-airfoil distance is studied in section IV. Concluding remarks are drawn in section V.

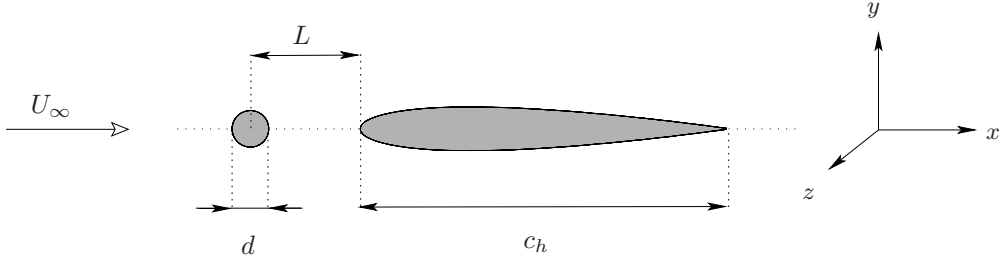


Figure 1. Sketch of the rod-airfoil configuration and of the coordinate system. The diameter of the rod is given by d while c_h is the chord length. The distance between the center of the rod and the leading edge of the airfoil is $L = c_h$. The freestream velocity is U_∞ .

II. Direct noise calculation of the rod-airfoil interaction on overset grids

II.A. Flow configuration

A sketch of the rod-airfoil setup and of the coordinate system is provided in figure 1. A NACA0012 airfoil is placed in a uniform flow with freestream velocity $U_\infty = 72 \text{ m}\cdot\text{s}^{-1}$, corresponding to a Mach number M_∞ equal to 0.2. A circular rod is located upstream the airfoil. The chord length is given by $c_h = 0.1 \text{ m}$ and the rod diameter d is such as $d = c_h/10$. The Reynolds numbers based on the chord length and the rod diameter are respectively given by $\text{Re}_{c_h} = 5 \times 10^5$ and $\text{Re}_d = 5 \times 10^4$. The gap L between the cylinder and the profile has been modified to investigate various flow regimes. Several simulations with the following values of L/d have hence been performed: $L/d = 0.07, 1, 1.5, 2.5, 3, 3.5, 4, 5, 6, 7, 7.5, 10, 10.5, 14, 17.5$. Particular attention has been paid to the case $L/d = 10$ which exactly corresponds to the experimental flow configuration of Jacob *et al.*¹⁹

II.B. Numerical methods and subgrid-scale modeling strategy

Owing to the complexity of the geometry encountered in the present study, an overset (also called Chimera) grid approach has been implemented.¹² Since the features of the overlap regions as well as the details of the interpolation procedure have to be established, the design of overset grids is a tedious task. Numerous grid assembly techniques and softwares are hopefully available.²¹ This work makes use of the library *Overture* designed by the Center for Applied Scientific Computing of the Lawrence Livermore National Laboratory.¹⁰

The three-dimensional unsteady compressible filtered Navier-Stokes equations are solved with the massively-parallel solver *Code_Safari*¹³ on the composite grid provided by the library *Overture*.¹⁰ For the purpose of aeroacoustic calculations, the need for highly accurate numerical methods has been recognized since the early stages of this computational field.²⁵ The large discrepancies between the length scales and the amplitudes of aerodynamic and acoustic fluctuations hence require the use of high-order schemes for both space and time discretizations. Following these guidelines, spatial derivatives are approximated using explicit 6th-order 7-point finite-differences. A selective filtering procedure is furthermore implemented in order to remove unwanted spurious perturbations. Spectral-like discrete filtering, based on a 6th-order 7-point stencil, is therefore applied to the flow variables.⁴ To keep accuracy at its highest level, Lagrangian interpolation is performed thanks to 4th-order polynomials.¹¹ Finally, time integration of the solution is carried out by a 4th-order 6-step low-storage Runge-Kutta scheme, whose coefficients have been optimized in the Fourier space.¹

Subgrid-scale modeling is performed using explicit filtering of the flow variables. The dissipation provided by the unresolved scales is thus taken into account by removing energy at the smaller scales, close to the grid cut-off.⁵

II.C. Grid design

The computational domain is discretized by eight different structured meshes. The resulting composite grid allows to accurately capture the turbulent flow development as well as the radiated sound field.

A sketch of the rod-airfoil multi-grid is presented in figure 2. Following the works of Boudet *et al.*⁸ or Greschner *et al.*¹⁵ the domain is taken to be periodic in the spanwise direction and extends over 0.3 chord-length. Around the rod and the airfoil, body-fitted curvilinear meshes have been constructed (grid #1 and

Table 1. Detailed characteristics for each mesh of the composite grid.

grid #	type	node number	typical mesh size (m)
1	rod	$500 \times 91 \times 45$	5×10^{-4}
2	airfoil	$400 \times 121 \times 45$	10^{-4}
3	aerodynamic	$1224 \times 189 \times 29$	5×10^{-4}
4	sponge zone	$238 \times 95 \times 29$	10^{-3}
5	intermediate	$1130 \times 189 \times 29$	10^{-3}
6	intermediate	$612 \times 142 \times 15$	2×10^{-3}
7	intermediate	$330 \times 118 \times 8$	4×10^{-3}
8	acoustic	$165 \times 471 \times 4$	10^{-2}

#2). Small mesh sizes have been chosen to ensure that all the features of wall turbulence are well reproduced. The first cell size normal to the wall is, in wall units, $\Delta y^+ \sim 2.5$ for the node on top of the rod. Above the middle of the airfoil, at $x/c_h = 0.5$, the mesh is such as $\Delta y^+ \sim 3$. The rod and the airfoil are surrounded by an aerodynamic Cartesian mesh in order to connect them (grid #3). Downstream the aerodynamic mesh lies a sponge zone used to attenuate turbulent motions before they hit the outflow boundary condition (grid #4). An acoustic mesh (grid #8) is also present to propagate sound waves to the far field. The mesh size is given by $\Delta x = \Delta y = \Delta z = 8.5 \times 10^{-2} c_h$ so that the cut-off wavelength of the grid corresponds to a cut-off Strouhal number equal to $fd/U_\infty \sim 1.4$, *i.e.* $f = 10000$ Hz. In-between the aerodynamic and the acoustic meshes (grid #3 and #6, respectively) intermediate meshes (grid #5, #6 and #7) have been placed to perform a smooth transition between the mesh sizes of the aerodynamic and acoustic domains. To avoid stiff mesh size jumps, only mesh coarsening by an approximate factor of two is used. It should be also noted that the spanwise mesh size is also varied in order to obtain mesh cells with an aspect ratio close to 1 in every direction.

The characteristics of the composite grid are compiled in table 1. The total number of mesh points is approximately 20×10^6 . One may observe that there are two orders of magnitudes between the typical mesh sizes in the aerodynamic region and the one in the far-field acoustic domain. Such a mesh jump is furthermore achieved in a smooth manner thanks to the grid overlapping technique. It is worth noting that most of the grid nodes are clustered inside the aerodynamic region. The discretization of the far-field (grid #8) indeed only requires 1.5% of the total number of mesh points.

In order to modify the gap between the rod and the airfoil, the grid around the cylinder (grid # 1) is simply shifted in the streamwise direction and the interpolation nodes are updated according to the new location of the mesh. For all the calculations, the domain extends over $[-4c_h; 10c_h] \times [-20c_h; 20c_h] \times [-0.15c_h; 0.15c_h]$. Two-dimensional views of the 3D grid obtained for the gap $L/d = 1$ are proposed in figure 3. The whole domain, presented in figure 3.a, covers a large fluid volume, including the acoustic far-field. A close-up view of the aerodynamic region is plotted in figure 3.b where the overlap between the cylindrical grid and the elliptic grid surrounding the profile is clearly visible. The interpolation nodes can be seen in figure 3.c. One may remark that the geometry of the mesh around the cylinder as well as the corresponding interpolation points have been adjusted in order to take account of the non-penetrating wall boundary conditions around the airfoil.

The time step $\Delta t \sim 6.5 \times 10^{-8}$ s corresponds to a Courant-Friedricks-Levy number equal to 0.8. To ensure statistical convergence, the simulations are run over 6×10^5 iterations on 256 processors.

III. Reference calculation - Solver validation

III.A. Overview of the flow field

The flow development as predicted by the numerical simulation is first investigated in a qualitative manner. Snapshots of the unsteady flow field are presented and discussed in order to determine whether the gross features of the flow physics are indeed well reproduced.

The turbulent flow development is illustrated in figure 4.a where the instantaneous snapshot of the

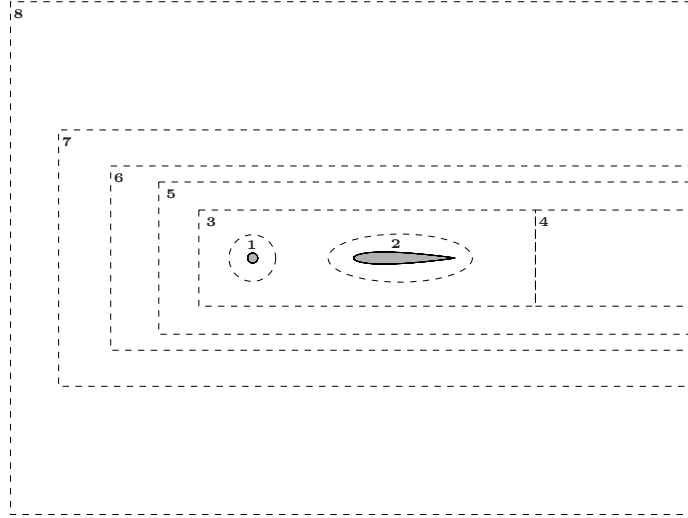


Figure 2. Sketch of the composite grid for the present rod-airfoil flow configuration (figure not to scale, overlapping regions not represented, recall that the grid is three-dimensional and has a spanwise extent in the z -direction). 1: rod mesh, 2: airfoil mesh, 3: aerodynamic mesh, 4: sponge zone, 5, 6, 7: intermediate meshes, 8: acoustic mesh.

magnitude of the velocity field, taken in the central plane of the computational domain, is plotted. It is seen that turbulence ignition is indeed achieved by the rod and that the development in the near-wall region of unsteady motions eventually leads to the periodic shedding of large scale organized vortices in the wake of the cylinder. Due to the flow three-dimensionalization, smaller turbulent scales are also visible.

An overview of the radiated acoustic field is proposed in figure 4.b, where a snapshot of the pressure fluctuations in the central plane is plotted. A tonal noise component, associated with the periodic impingement of the rod wake on the airfoil, is clearly visible on either side of the rod-airfoil setup.

III.B. Mean flow field

Some mean flow quantities, namely mean velocities and turbulence intensities, are now faced with hot-wire data to check the consistency of the present results. It should be noted that Jacob *et al.*¹⁹ pointed out that during their experiments the rod and the airfoil were not perfectly aligned. The rod is indeed a few millimeters (a few percent of the chord length) off in the transverse direction. Due to this bias into the experimental flow setup, discrepancies can be expected. One may nonetheless consider that the measurements of Jacob *et al.*¹⁹ provide reliable references of the overall magnitude of the mean flow quantities.

The mean streamwise velocity \bar{u}/U_∞ is represented in figure 6 as a function of the transverse coordinate y/c_h . Three streamwise locations, as shown in figure 5, referred to as section [A] ($x/c_h = -0.255$), section [B] ($x/c_h = 0.25$) and section [C] ($x/c_h = 1.1$) are plotted in figures 6.a, 6.b and 6.c, respectively. The experimental data of Jacob *et al.*¹⁹ are presented for comparison. In-between the rod and the airfoil, in figure 6.a, a good collapse between the present results and the experimental data is observed. The wake width as well as the velocity defect at the center of the wake are well reproduced. Further downstream, above the profile, it is seen in figure 6.b that there is a fair agreement between the numerical data and the hot-wire profile. At this location the calculation turns out to overestimate the streamwise mean flow but the overall amplitude is nonetheless well predicted. Finally, the mean streamwise velocity in the wake of the airfoil, presented in figure 6.c, is also consistent with the hot-wire measurements. The gap between the experiments and the simulation is rather large for $y/c_h > 0$ but a very good collapse is visible for negative transverse locations. Recall that the experimental setup is not symmetric so that the hot-wire measurements are consequently not symmetric too.

The turbulent intensity $\sqrt{u'u'}/U_\infty$ based on the mean streamwise velocity fluctuations is depicted in figure 6 as a function of the transverse coordinate y/c_h , for three streamwise locations : section [A] in figure 6.d, section [B] in figure 6.e and section [C] in figure 6.f. The experimental data of Jacob *et al.*¹⁹ are also provided to assess the present LES results. Downstream the cylinder, in figure 6.d, the turbulent activity in the center of the wake is slightly overestimated by the present calculation but the overall agreement is

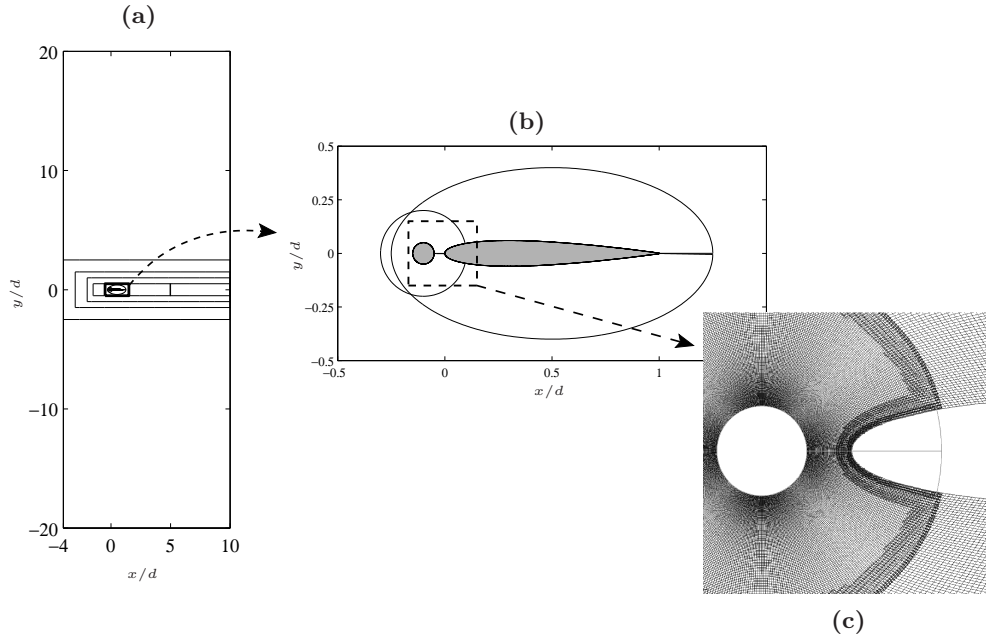


Figure 3. Two-dimensional view of the calculation domain for $L/d = 1$ (recall that the grid has a spanwise extent in the z -direction). (a) Overview of the whole domain, (b) close-up view in the aerodynamic region in the neighborhood of the rod and the airfoil, and (c) view of the meshes around the rod and the airfoil and of the interpolation points (represented by bold dots at the mesh frontiers) used to exchange data between the two grids.

good and few discrepancies can be seen between the two sets of data. In figure 6.e, the turbulent intensity above the airfoil provided by the simulation is slightly larger than that of the experiments. The error remains however within a few percents. Further downstream, in figure 6.f, turbulence activity in the wake of the airfoil is correctly predicted. In particular, as it was already reported for the mean streamwise velocity in figure 6.c, a better collapse with the reference data is observed for negative transverse locations.

III.C. Radiated acoustic field

The time evolution of the pressure fluctuations p' obtained at the location $(x/c_h, y/c_h) = (0, 18.5)$ in the far-field, as shown in figure 5, is presented in figure 7.a as a function of the normalized time tU_∞/d . It is seen that the signal is dominated by periodic oscillations with amplitudes slightly modulated in time. This tone noise is associated to the sound radiated by the periodic impingement of vortical structures on the airfoil leading edge.

The power spectral density (PSD) of the far-field pressure fluctuations is provided in figure 7.b as a function of the Strouhal number $St = fd/U_\infty$ based on the cylinder diameter. The experimental data of Jacob *et al.*¹⁹ are also plotted for comparison. A good collapse between numerical and experimental results is observed even though the half-width of the pic is overestimated. This trend is likely to be due to the discrepancies between the length of the signals of the simulation and of the experiments. Numerical calculation indeed provide relatively short time-resolved data. Nonetheless, as expected, the calculated spectrum exhibit a strong tonal component at the vortex shedding frequency and the predicted Strouhal number shows a very good agreement with the reference data. In addition the pressure level radiated by the harmonic pic is well reproduced. The gap between the simulation and the experiments remains small, about 4 dB.

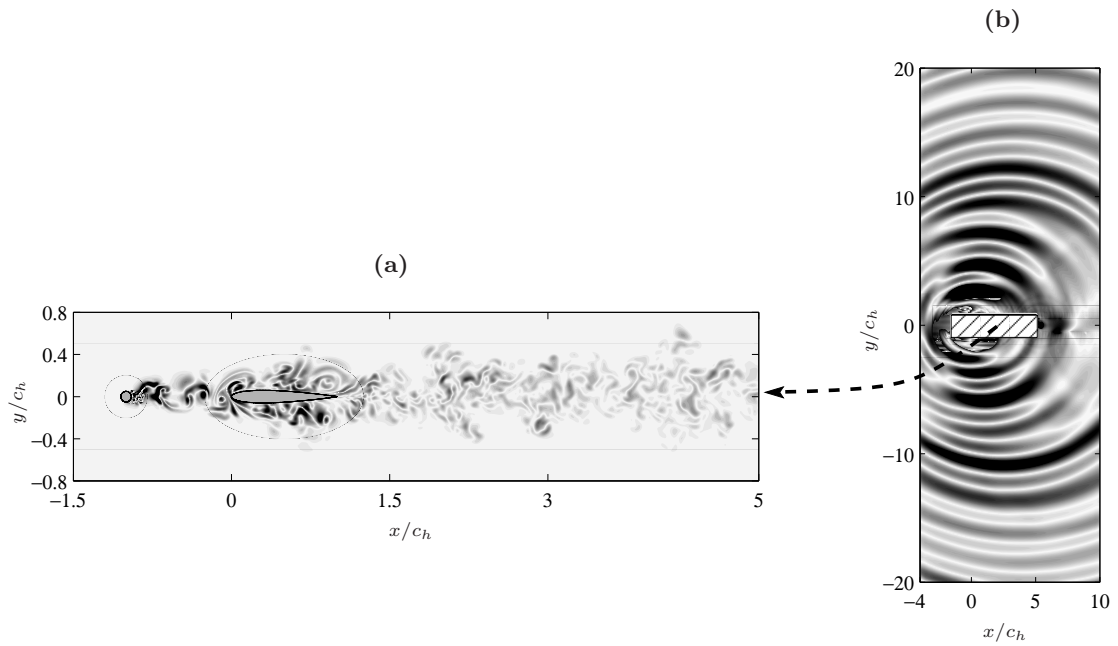


Figure 4. (a) Snapshot of the modulus of the unsteady spanwise velocity field $|u_z|$ in the central plane of the computational domain for $L/d = 10$. Colorscale from 0 (white) to $0.3U_\infty$ (black). Gray surfaces represent solid bodies. (b) Snapshot of the magnitude $|p'|$ of the fluctuating pressure field in the central plane of the computational domain. Colorscale from 0 Pa (white) to 50 Pa (black). The dashed area corresponds to the flow region presented on the left.

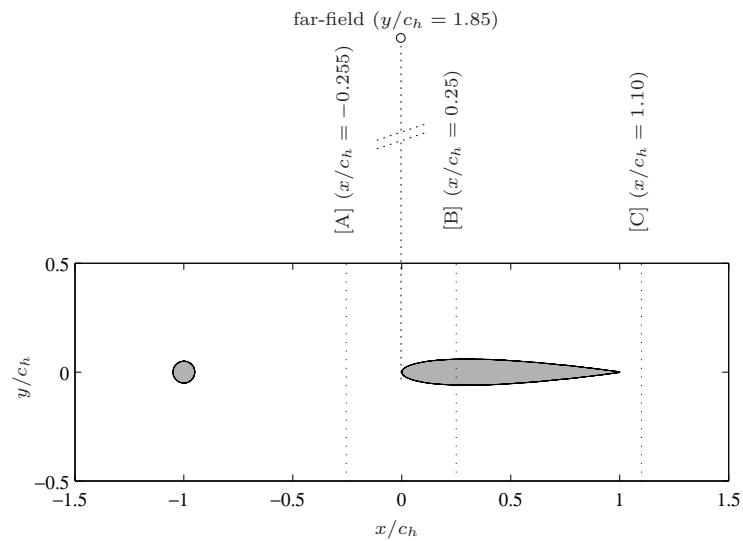


Figure 5. Sketch of the measurement locations for the reference flow configuration with $L/d = 10$. The figure is to scale.

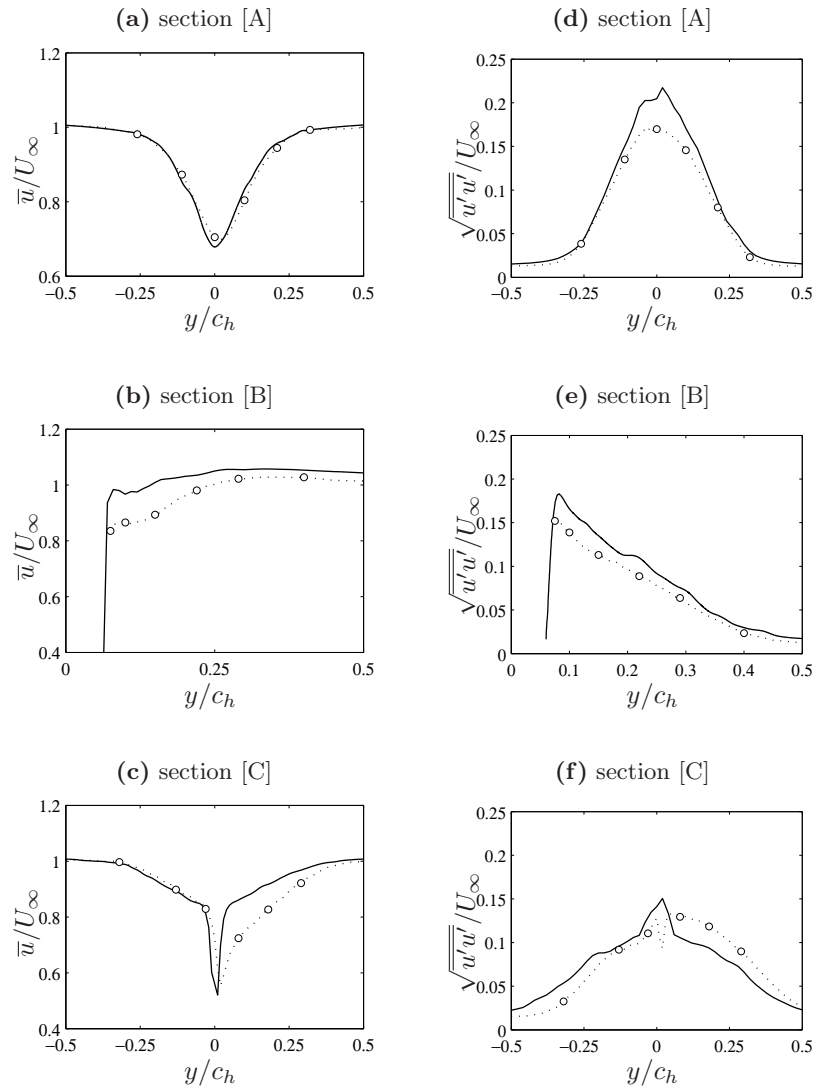


Figure 6. (a–c) Mean streamwise velocity \bar{u}/U_∞ as a function of the transverse position y/c_h , and (d–f), mean streamwise turbulent intensity $\sqrt{u'u'}/U_\infty$ as a function of the transverse position y/c_h , for various streamwise locations. —, present LES; $\cdots \circ \cdots$, experimental data.¹⁹

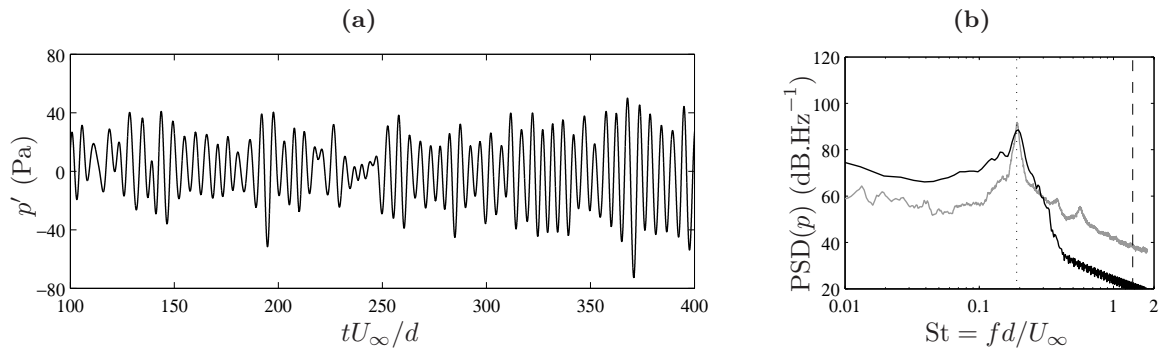


Figure 7. (a) Pressure fluctuation history in the far-field for an observer normal to the flow at a distance $R = 18.5c_h$ from the airfoil leading edge. (b) Power spectral density of the pressure perturbations measured in the far-field for an observer normal to the flow at a distance $R = 18.5c_h$ from the airfoil leading edge. The present LES results (black plot) are compared to the data provided by the experiments of Jacob *et al.*¹⁹ (gray plot). The dotted line indicates the expected Strouhal number $St = 0.19$ of the vortex-shedding frequency behind the cylinder. The dashed line represents the mesh cut-off Strouhal number $St = 1.39$ in the far-field grid.

IV. Distance influence

IV.A. Flow regimes

Several snapshots of the spanwise vorticity are displayed in figure 8 for some values of L/d . For $L/d = 0.07$ and $L/d = 0.25$, it is observed the two separated shear layers do not interact and reattach on the airfoil. For $L/d = 0.35$, the flow regime changes. Now, the two separated shear layers have some interaction and do not reattached directly on the airfoil. But no regular vortex shedding appears. For $L/d = 0.65$, the expected eddies due to the vortex shedding behind the rod are present.

These results are confirmed by figure 9 which shows the mean streamwise turbulent intensity fields in the same configurations. For $L/d = 0.07$ and $L/d = 0.25$, it is observed that no high turbulent intensity exists behind the rod. Significant turbulence levels are only present in the two separated shear layers that do not interact and reattach directly on the airfoil.

So it appears that for $L/d = 0.35$, a transition in the flow regimes occurs between a “shear layer regime” ($L/d < 0.35$) and a “wake regime” ($L/d > 0.35$).

IV.B. Flow statistics

IV.B.1. Pressure distribution

The pressure coefficient $C_p = (p - p_\infty)/(2\rho U_\infty^2)$ around the rod and the airfoil are presented in figure 10.a and 10.b, as a function of the angle θ with the upstream direction for the cylinder, and with respect to the streamwise location x/c_h for the profile. Data obtained for all the spacings L are plotted.

It is first observed in figure 10.a that all the curves have a similar shape, typical of the flow around a cylinder. Starting from a value of 1 at the front stagnation point ($\theta = 0$ deg), the pressure coefficient decreases further downstream and eventually reaches a minimum for θ in-between 60 deg and 80 deg depending on the gap L . At this point, separation of the shear-layer occurs. Behind this location on the rod surface, the pressure coefficient exhibit a plateau value ranging from -1.5 to -0.5 . For the single cylinder, corresponding to $L/d = \infty$, the pressure distribution shows a good collapse with the experimental measurements of Igarishi,¹⁷ obtained for a rod at a slightly lower Reynolds number $Re_d = 3.5 \times 10^4$.

As concern the pressure coefficient around the airfoil in figure 10.b, for large gaps, $L/d > 7.5$, the pressure distribution shows strong similarities with the one of a single airfoil. The coefficient C_p , which is positive at the leading edge, decreases, becomes negative and reaches a minimum value around $x/c = 0.2$. In the pressure recovery region, for $x/c > 0.2$, the pressure coefficient increases down to the trailing edge where it is close to 0.

For smaller gaps, $L/d < 5$, the main discrepancies are seen in the neighborhood of the leading edge. The downstream part of the curves, for $x/c > 0.4$, is indeed very similar to the one observed for larger gaps. In the upstream part of the plots, the pressure distribution shows a low negative coefficient at the leading edge and a maximum value at the streamwise location x/c of the reattachment point of the separated shear layer from the upstream rod. In addition, for small spacings, the pressure coefficient at the rear stagnation point of the rod is almost the same as the pressure coefficient at the leading edge of the profile. This trend is highlighted in figure 11 where the coefficients C_p , calculated rear the cylinder and in front of the airfoil, are plotted as functions of the gap L/d . As pointed out, for large gaps, the two coefficients are different but when the spacing is small enough, for $L/d < 3.5$ in the present results, the values of the pressure coefficients shows a good collapse around the value $C_p = -0.5$. This fact indicates that the flow undergoes few modifications in the gap between the rod and the airfoil.

IV.B.2. Drag coefficient

The drag coefficient $C_d = \int_0^\pi C_p \cos \theta d\theta$ obtained by integration of the pressure distribution around the cylinder is shown in figure 12.a as a function of the gap L/d . For the single cylinder ($L/d = \infty$) the drag coefficient, equal to 1.2, has a value in good agreement with experimental measurements at the same Reynolds number.²⁸ The coefficient then decreases gradually in inverse proportion to the gap between the rod and the airfoil, and reaches a minimum for $L/d = 10$. At $L/d = 6.5$, the drag undergoes a step increase and reaches the value $C_d = 1.15$. For smaller separation distances the coefficient continues to diminish but it nonetheless reaches another peak value for the spacing $L/d = 3.5$, with $C_d = 0.9$. From $L/d = 3.5$ to $L/d = 3$ a stepwise

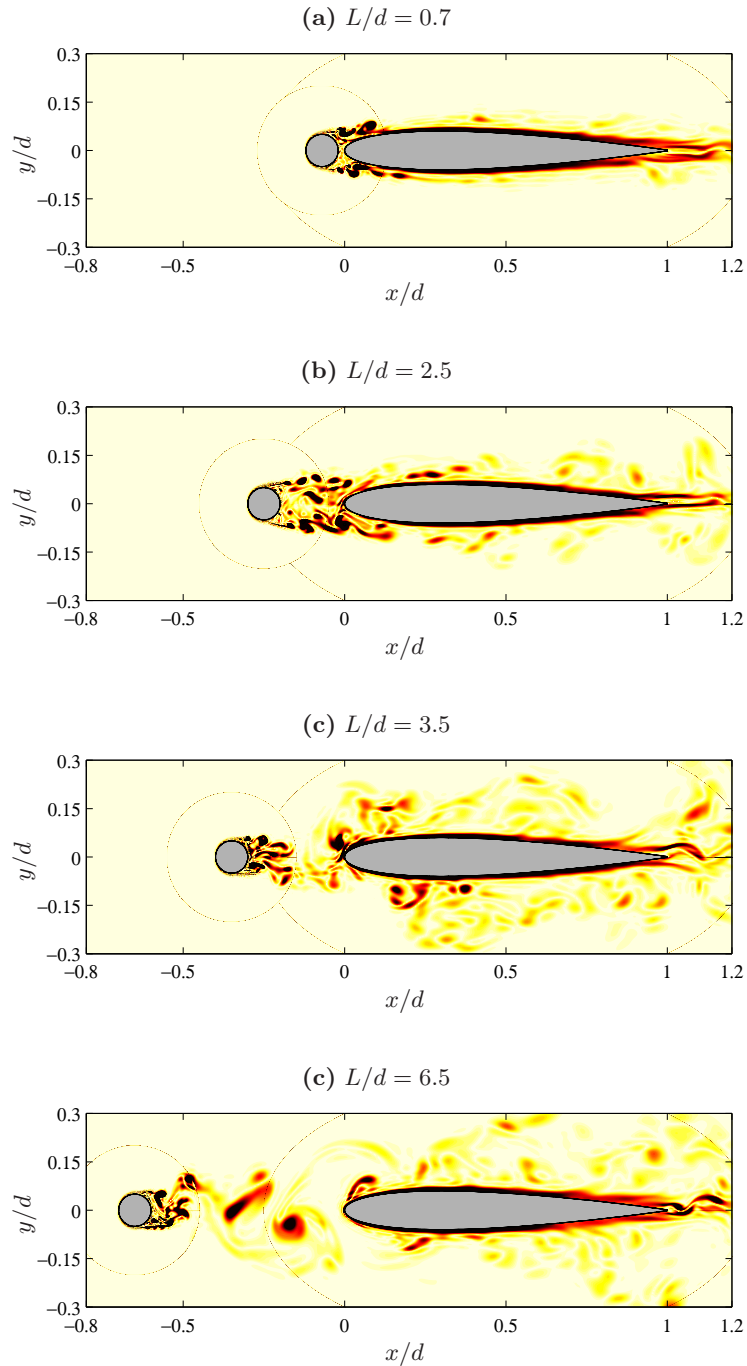


Figure 8. Snapshot of the modulus of the spanwise vorticity component $|\omega_z|d/U_\infty$ in the central plane of the computational domain for selected values of the gap L/d . Colorscale from 0 (white) to 5 (black). Gray surfaces represent solid bodies.

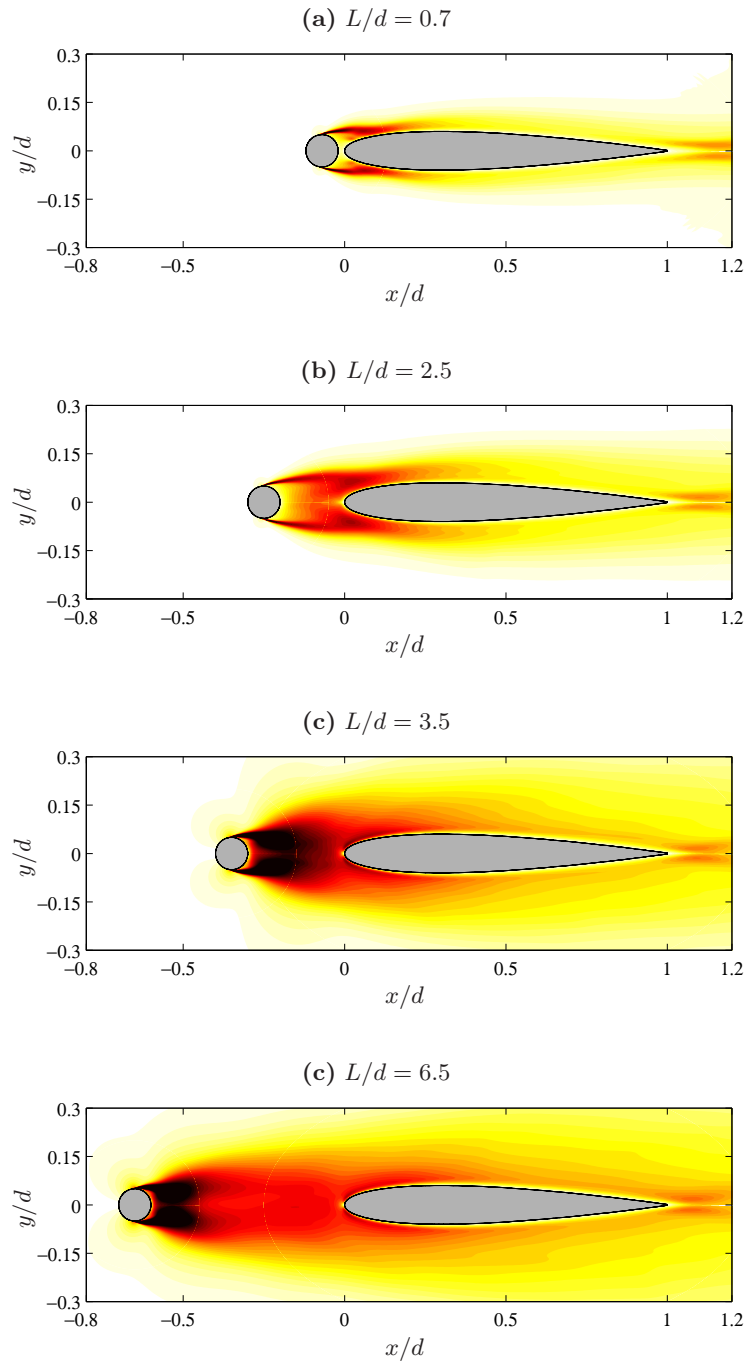


Figure 9. Mean streamwise turbulent intensity $\sqrt{u'u'}/U_\infty$ in the central plane of the computational domain for selected values of the gap L/d . Colorscale from 0 (white) to 0.4 (black). Gray surfaces represent solid bodies.

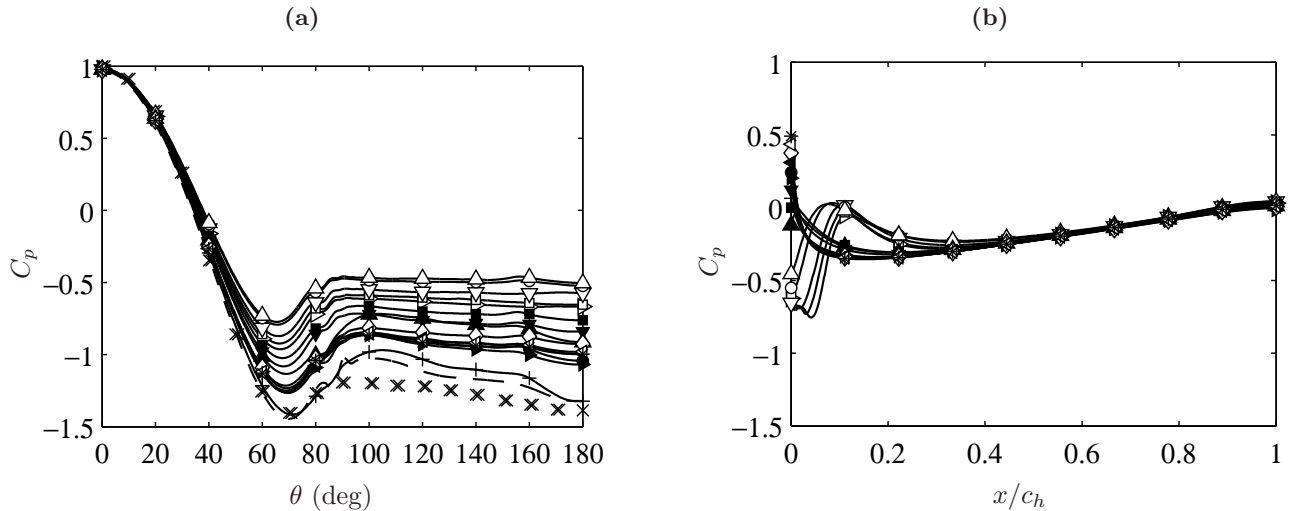


Figure 10. Distribution of the pressure coefficient C_p around (a) the rod and (b) the airfoil, for various values of the gap L/d . \triangleright , $L/d = 0.7$; \square , $L/d = 1$; ∇ , $L/d = 1.5$; \circ , $L/d = 2.5$; \triangle , $L/d = 3$; \blacktriangle , $L/d = 3.5$; \blacksquare , $L/d = 4$; \blacktriangledown , $L/d = 5$; $+$, $L/d = 6.5$; *blacktriangleright*, $L/d = 7$; \bullet , $L/d = 7.5$; \diamond , $L/d = 10$; \blacktriangleleft , $L/d = 1.05$; \blacktriangleleft , $L/d = 14$; $*$, $L/d = 17.5$; $---$, $L/d = \infty$; \times , experimental data for a single cylinder at $Re_d = 3.5 \times 10^4$.¹⁷

decrease is visible and corresponds to a suddain change in the flow regime. At $L/d = 3$ the drag coefficient is about 0.7 and smoothly increases to 0.9 when the gap is reduced down to $L/d = 0.7$.

In a similar manner, the drag coefficient $C_d = 2 \int_0^1 C_p(dy/dx) d(x/c_h)$ of the airfoil is provided in figure 12.b. The value $C_d = 0.0072$, for $L/d = \infty$, corresponds to a single NACA0012 airfoil and has been obtained by interpolating the experimental data of Sheldahl & Klimas²² with respect to the Reynolds number.

As soon as there is a rod upstream the airfoil, the drag coefficient becomes negative so that the drag acts as a thrust on the profile. The magnitude of this upstream-oriented force is lowered when the gap between the two bodies decreases. The minimum value of the coefficient is observed for the smaller spacing studied in this work, $L/d = 0.7$ with $C_d = -0.047$. This value of the drag coefficient is, in magnitude, about six times larger than the drag for a single profile. For spacings larger than $L/d = 3.5$, the variations of the drag coefficient are seen to be relatively small. A minimum value is however still observed for $L/d = 6.5$ which corresponds to the gap value leading to a maximum of drag on the upstream cylinder. When the distance between the rod and the airfoil is smaller than $L/d = 3.5$ a sharp decrease of the drag acting on the airfoil is clearly observed, with a coefficient C_d equal to -0.006 for $L/d = 3.5$ and falling down to -0.047 for $L/d = 0.7$.

At this point, two main flow regimes seem to emerge and $L/d = 3.5$ appears to be the critical spacing where the transition occurs. For spacings larger than $L/d = 3.5$, the flow undergoes a “wake mode”: the gross features of the flow in the wake of the rod are not modified and periodic vortex shedding is likely to be maintained. For gaps smaller than $L/d = 3.5$, a “shear mode” is observed. The airfoil has then a significant impact on the turbulent flow development around the cylinder. In addition, the distance $L/d = 6.5$ also seems to lead to a large value of the drag coefficient of the rod, through the main features of the flow development seem to those of the “wake mode”.

IV.C. Acoustic field

IV.C.1. Overview

An overview of the radiated acoustic field is provided in figure 13 where the magnitude of the pressure fluctuations $|p'|$ is plotted in the central plane of the computational domain, for a few values of the gap, $L/d = 0.7; 2.5; 3.5; 5; 6.5; 10$.

One may first observed that for separation distances above the critical gap $L/d = 3.5$, in figures 13.c to 13.f, a well-organized tonal noise component is visible for all the configurations, on both sides of the rod-airfoil. The sound pressure level is particularly high for a separation $L/d = 3.5$ and is maximum when

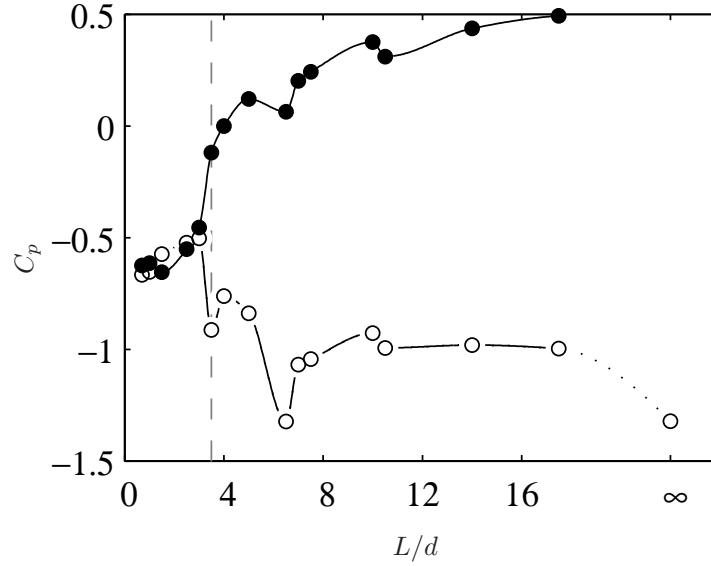


Figure 11. Pressure coefficients C_p at the rear stagnation point of the rod ($\theta = 180$ deg), and at the leading edge of the airfoil ($x/c_h = 0$), as functions of the gap L/d . o, Rod; •, airfoil.

$L/d = 6.5$.

For spacings smaller than $L/d = 3.5$, in figures 13.a and 13.b, the magnitude of the pressure perturbations in the far field is lower. In addition, even though some acoustic wavefronts can be seen, the pressure field seems to be more chaotic than for the wake mode, when $L/d > 3.5$.

IV.C.2. Strouhal number and sound pressure level

The trends highlighted in the preceding section are further confirmed by the quantitative data provided in figure 14.

The Strouhal number $St = fd/U_\infty$ of the dominant harmonic pic is plotted against the separation distance L in figure 14.a. Note that for the gap $L/d = 1$, the pressure signal in the far-field was too chaotic and no major tonal component was found. There is consequently no data for the spacing $L/d = 1$. In a similar manner, the overall sound pressure level measured in the far field is provided in figure 14.b as a function of the parameter L/d . The Strouhal number and the sound pressure level obtained for a single cylinder are also given for comparison.

As concern the Strouhal number in figure 14.a, the presence of the airfoil in the far wake of the cylinder turns out to slightly increase the frequency of the vortex shedding. For a single cylinder at this Reynolds number, the Strouhal number is about 0.18 but for separation distances L/d inbetween 10 and 17.5, this number is closer to 0.20. An interesting point is that below $L/d = 10$ the frequency of the main tonal noise component progressively decreases down to a Strouhal number $St = 0.11$ for $L/d = 0.25$. The curve slope is in addition significantly stiffer below the critical gap $L/d = 3.5$. Finally, it is seen that for smaller spacings the Strouhal number increases again to reach the value $St = 0.16$ for $L/d = 0.7$.

It is worth noting that very similar results have been found by Igarishi¹⁷ for the case of two tandem cylinders. In this two cylinder configuration, the critical gap is about $L/d = 3$ but the Strouhal number of the velocity fluctuations in the wake of the first cylinder exhibits similar trends: the frequency is lower when the gap L/d is smaller, it then undergoes a sharp decrease below the critical gap but for small enough separation distances the Strouhal number increases again.

For the overall sound pressure level (OSPL) represented in figure 14.b, the magnitude of the radiated pressure field is larger when the distance between the two bodies is narrowed. In the “wake mode” region, for $L/d = 3.5$, starting from an OSPL of 115 dB for the single cylinder, levels as high as 125 dB and 126 dB are measured for the gaps $L/d = 3.5$ and $L/d = 6.5$, respectively. In this case, adding the airfoil makes the flow noisier. To the contrary, once the “shear mode” is ignited, the profile downstream the rod leads to radiation levels lower than those measured for a single cylinder. For $L/d = 3.5$, the OSPL undergoes a

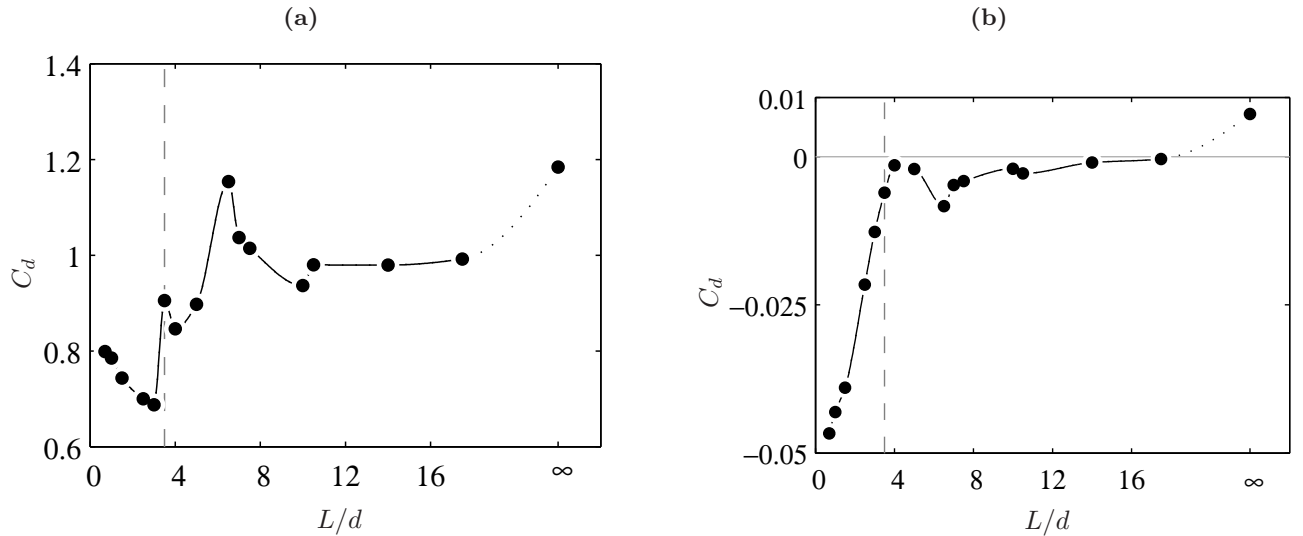


Figure 12. Drag coefficients C_d of, (a), the rod and (a), the airfoil, as functions of the gap L/d .

step-like decrease between $L/d = 3.5$ and $L/d = 3$ with a 16 dB gap between the two configurations. Then, the OSPL decreases down to 94 dB when the gap is reduced to $L/d = 0.7$.

V. Conclusion

In the present paper, direct noise calculation of the sound sources of a rod-airfoil flow configuration has been performed. Using the specific solver *Code_Safari*,¹³ the large-eddy simulation of the compressible Navier-Stokes equations using spectral-like numerical methods on a set of overlapping grids permitted to determine the turbulent flow development as well as the radiated sound field in a single calculation. Detailed comparisons to the experimental data of Jacob *et al.*¹⁹ have been carried out to assess the consistency of the present computation. A good agreement between the reference data and the predicted results has been shown for the turbulence statistics and for the quasi-tonal sound radiation observed in the far-field.

The influence of the distance between the cylinder and the profile has then been performed. Based on both aerodynamic and acoustic flow data, two turbulent flow developments have been identified: the so-called “wake” and “shear” modes. The separation distance $L/d = 3.5$ in addition turned out to be the critical spacing where the mode transition occurred. The investigation of the acoustic far-field demonstrated that the overall sound pressure level and its dominant tonal noise component are significantly affected by the flow mode.

This study therefore demonstrates that the use of high-order discretization tools on overlapping structured grids permits to perform the direct noise calculation of the sound sources associated to the turbulent flow development around multiple bodies is feasible and yields accurate results.

As pointed out, among the numerous branches of the aeroacoustic computation field, direct calculation of the radiated acoustic is particularly reliable since it does not require any sound source modeling. It produces comprehensive data which can help understanding the flow physics of sound generation processes in turbulent flows.

Acknowledgments

This work is supported by the “Agence National de la Recherche” under the reference ANR-06-CIS6-011 (project “STURM4”).The authors wish to thank Dr. Bill Henshaw for his valuable recommendations concerning the overset strategy.

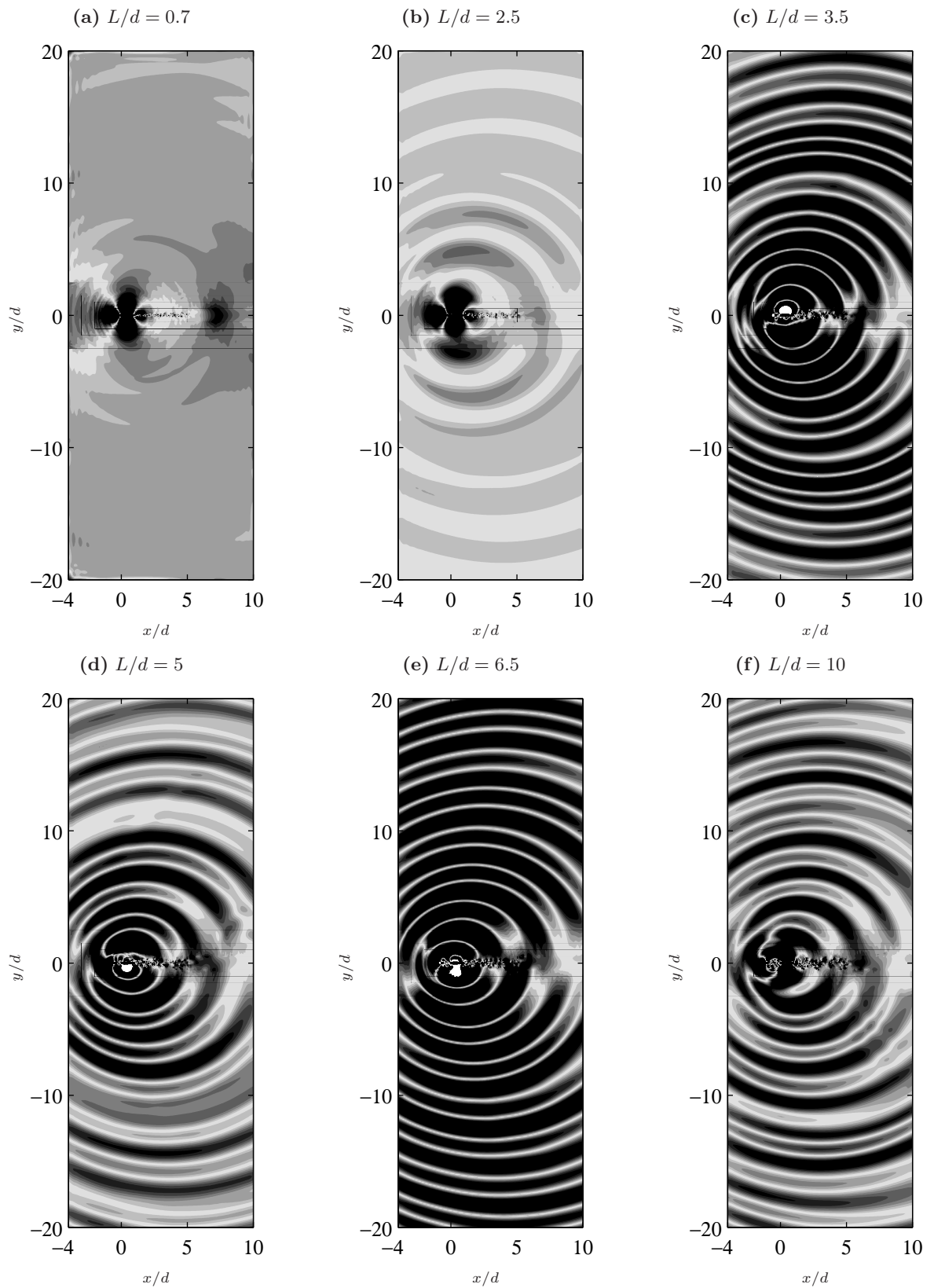


Figure 13. Snapshot of the magnitude $|p'|$ of the fluctuating pressure field in the central plane of the computational domain for selected values of the gap L/d . Colorscale from 0 Pa (white) to 50 Pa (black). Gray surfaces represent solid bodies.

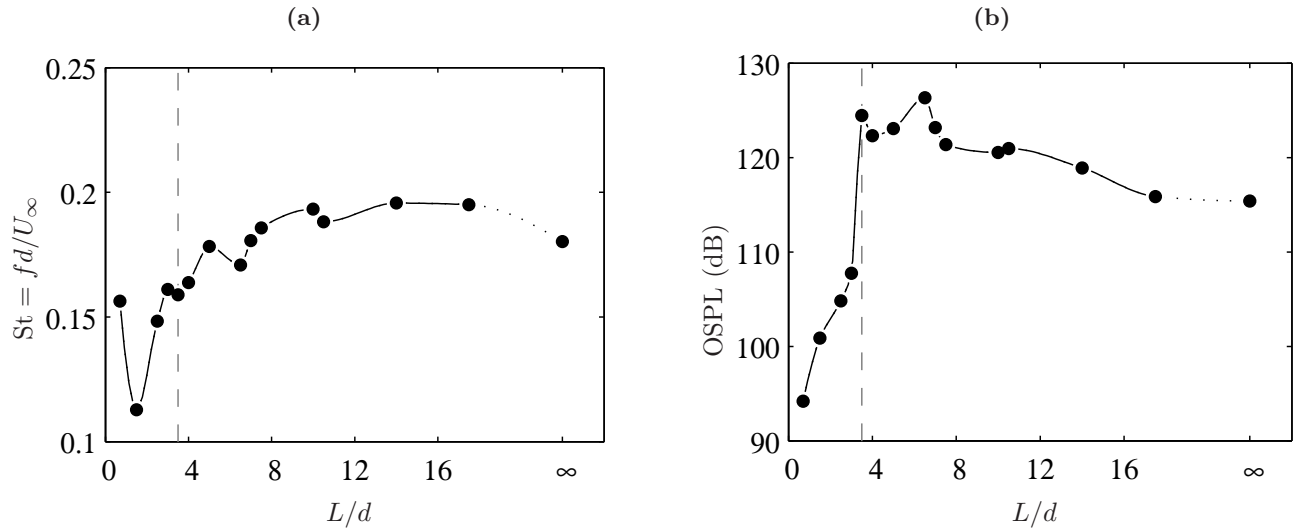


Figure 14. Characteristics of the acoustic far-field as functions of the gap L/d . (a), Strouhal number $St = fd/U_\infty$ of the dominant harmonic pic, and (b), overall sound pressure level (OSPL) of the corresponding signal.

References

- ¹Berland, J., Bogey, C., Bailly, C., Low-dissipation and low-dispersion fourth-order Runge-Kutta algorithm, *Comput. Fluids*, **35**, 1459-1463 (2006)
- ²Berland, J., Bogey, C., Bailly, C., Numerical study of screech generation in a planar supersonic jet, *Phys. Fluids*, **19**, #075105 (2007)
- ³Berland, J., Lafon, P., Crouzet, F., Daude, F., Bailly, C., Numerical insight into sound sources of a rod-airfoil flow configuration using direct noise calculation, 16th AIAA/CEAS Aeroacoustics Conference, 7-9 june, Stockholm, Sweden, AIAA Paper 2010-3705 (2010)
- ⁴Bogey, C., Bailly, C., A family of low dispersive and low dissipative explicit schemes for flow and noise computations, *J. Comput. Phys.*, **194**, 194-214 (2004)
- ⁵Bogey C., Bailly C., Large eddy simulations of round free jets using explicit filtering with/without dynamic Smagorinsky model, *Int. J. Mass Transfer*, **27**, 603 (2006).
- ⁶Bogey C., Bailly C., An analysis of the correlations between the turbulent flow and the sound pressure fields of subsonic jets, *J. Fluid Mech.*, **583**, 71 (2007).
- ⁷Bogey C., Bailly C., Turbulence and energy budget in a self-preserving round jet, *J. Fluid Mech.*, **627**, 129 (2009).
- ⁸Boudet J., Grosjean N., Jacob M.C., Wake-airfoil interaction as broadband noise source: a large-eddy simulation study, *Int. J. Aeroacoustics*, **4**(1), 93 (2005)
- ⁹Casalino, D., Jacob M.C., Roger M., Prediction of rod-airfoil interaction noise using the Ffowcs-Williams Hawkins analogy, *AIAA J.*, **41**(2), 182-191 (2003)
- ¹⁰Chessirre, G., Henshaw, W.D., Composite overlapping meshes for the solution of partial differential equations, *J. Comput. Phys.*, **90**, 1-64 (1990)
- ¹¹Daude F., Emmert T., Lafon P., Crouzet F., Bailly C., A high-order algorithm for compressible LES in CAA applications, *Proceedings of the 14th AIAA/CEAS Aeroacoustics Conference*, 5-7 may, Vancouver, Canada, USA, AIAA Paper 2008-2873 (2008)
- ¹²Delfs, J.W., An overlapped grid technique for high resolution CAA schemes for complex geometries, *Proceedings of the 7th AIAA/CEAS Aeroacoustics Conference and Exhibit*, Maastricht, Netherlands, May 28-30, AIAA-Paper 2001-2199 (2001)
- ¹³Emmert, T., Lafon, P. & Bailly, C., Numerical study of self-induced transonic flow oscillations behind a sudden duct enlargement, *Phys. Fluids*, **21**, 106105 (2009)
- ¹⁴Ffowcs Williams, J.E., Hawkins, D.L., Sound generated by turbulence and surfaces in arbitrary motion, *Phil. Trans. Roy. Soc.*, **A264**(1151), 321-342 (1969)
- ¹⁵Greschner B., Thiele F., Jacob M.C., Casalino D., Prediction of sound generated by a rod-airfoil configuration using EASM DES and the generalised Lighthill/FW-H analogy, *Comput. Fluids*, **27**, 402-413 (2008)
- ¹⁶Homicz G.F., George A.R., Broadband and discrete frequency radiation from subsonic rotors, *J. Sound Vib.*, **36**(2), 151 (1974)
- ¹⁷Igarashi T., Characteristics of the flow around two circular cylinders arranged in tandem (1st report), *Bulletin of the JSME*, **24**, 323 (1981)
- ¹⁸Kato C., Iida A., Takano Y., Fujita H., Ikegawa M., Numerical prediction of aerodynamic noise radiated from low Mach turbulent wake, *Proceedings of the 31st AIAA Aerospace Sciences Meeting and Exhibit*, 11-14 january, Reno, NV, USA, AIAA Paper 93-0145 (1993)

- ¹⁹Jacob M.C., Boudet J., Casalino J., Michard M., A rod-airfoil experiment as benchmark for broadband noise modeling, *J. Theoret. Comput. Fluid Dyn.*, **19**(3), 171 (2005).
- ²⁰Lighthill, M., On sound generated aerodynamically, I, general theory, *Proc. Roy. Soc. London*, **A-211**, 564-587 (1952)
- ²¹Prewitt, N.C., Belk, D.M., Shyy, W., Parallel computing of overset grids for aerodynamic problems with moving objects, *Prog. Aerosp. Sci.*, **36**, 117-172 (2000)
- ²²Sheldahl R., Klimas P., Aerodynamic characteristics of seven symmetrical airfoil sections through 180-degree angle of attack for use in aerodynamic analysis of vertical axis wind turbines, Sandia National Laboratories, Technical report SAND80-2114 (1981)
- ²³Sherer, S.E., Scott, J.N., High-order compact finite-difference methods on general overset grids, *J. Comput. Phys.*, **210**(2), 459-496 (2005)
- ²⁴Takagi, Y., Fujisawa, N., Nakano, T., Nashimoto, A., Cylinder wake influence on the tonal noise and aerodynamic characteristics of a NACA0018 airfoil, *J. Sound Vib.*, **297**, 563-577 (2006)
- ²⁵Tam, C.K.W., Computational aeroacoustics: issues and methods, *AIAA J.*, **33**, 1788-1797 (1995)
- ²⁶Tam C.K.W., Dong Z., Radiation and outflow boundary conditions for direct computation of acoustic and flow disturbances in a nonuniform mean flow, *J. Comput. Acoust.*, **4**, 175 (1996)
- ²⁷Wang, M., Freund, J.B., Lele, S.K., Computational prediction of flow-generated sound, *Ann. Rev. Fluid Mech.*, **38**, 483-512 (2006)
- ²⁸Williamson C.H.K., Vortex dynamics in the cylinder wake, *Ann. Rev. Fluid Mech.*, **28**, 477 (1996).